Experimental Evaluation of a SiPM-Based Scintillation Detector for MR-Compatible SPECT Systems

Paolo Busca, Michele Occhipinti, Paolo Trigilio, Giulia Cozzi, Carlo Fiorini, Claudio Piemonte, Alessandro Ferri, Alberto Gola, Kálmán Nagy, Tamás Bükki, and Jan Rieger

I. INTRODUCTION

IN RECENT years, multi-modality PET/MRI and SPECT/MRI systems are emerging in clinical and research applications aiming to provide simultaneous anatomical, functional and molecular information [1]. MRI offers high-resolution details of morphological structures with much better soft tissue contrast than that of conventional X-ray CT. Nuclear imaging techniques allow following functional metabolism with different advantages [2]. For example in small animal imaging, while PET has higher sensitivity, SPECT provides better spatial resolution and the possibility to use different radionuclides to demonstrate multiple biological processes simultaneously. In addition, SPECT radiotracers are typically longer lived and more readily accessible.

Usual requirements for SPECT detectors are good intrinsic spatial resolution to optimize the sensitivity-resolution trade-off, high energy resolution especially for applications where a lot of scatter can occur and adequate count rate capability, though less challenging than in PET, due to the presence of the collimator.

A simultaneous SPECT/MRI system could provide combined information to target different bio-markers and to label compounds with either diagnostic or therapeutic radionuclides. Therefore it has the potential to estimate internal radiation dose, important for the treatment planning of personalised radionuclide-based therapies.

The development of hybrid SPECT/MRI systems is still in its infancy, especially on the clinical side. First studies have been performed by using a pre-clinical SPECT system brought in close proximity to a low field (0.1 T) MRI for sequential acquisitions [3], [4]. Though the feasibility of SPECT/MRI was demonstrated, the instrument is not truly integrated and not compatible with high field MRIs.

Besides usual challenges for MRI integration in common with PET systems, such as need for a compact system, compatibility with the static magnetic field, robustness to radiofrequency pulses and rapidly switching gradient fields, SPECT has additional technical issues. The bulky material of collimators can lead to the generation of eddy currents, worsening the uniformity of the magnetic field. Moving and rotating parts can induce artefacts in MRI images, thus stationary scanners are preferred.

More recently, pre-clinical simultaneous SPECT/MRI systems have been developed by different groups exploiting arrays of pixelated CdTe and CdZnTe gamma detectors [5], [6], [7], [8]. These approaches offer excellent energy resolution due to direct conversion, optimal for the simultaneous use of multiple radionuclides, and sub-millimeter spatial resolution depending on the pixel size.

The rapid evolution of Silicon PhotoMultipliers (SiPMs) technology is replacing PhotoMultiplier Tubes in many applications including TOF-PET and is now qualifying this sensor
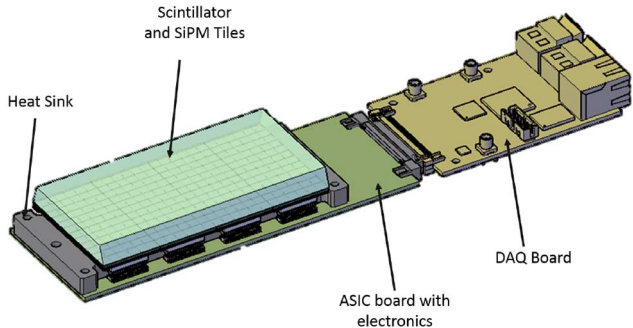
Fig. 1. Design of the photo-detection module (clinical system). For the preclinical system, only half of the camera (crystal and SiPMs) is mounted.

also for MRI-compatible SPECT applications with both monolithic and pixelated architectures. The use of analog and digital SiPMs for low energy imaging has already been reported for monolithic LYSO:Ce [9], pixelated CsI:Tl [10] and pixelated GaGG:Ce [11], [12] scintillators.

The monolithic solution carries some advantages over the pixelated approach, like high spatial resolution without compromising energy resolution and sensitivity, lower cost and simpler assembly. On the other hand, scintillation photons are distributed over several photo-detectors and the signal-to-noise ratio per channel is low, especially in a low-energy range, demanding low noise devices. Another drawback is related to the calibration procedure necessary for the equalization of several channels that requires dedicated procedures.

In this paper we present preliminary results in the development of a camera based on analog SiPMs to read a monolithic CsI:Tl scintillator, in the framework of the INSERT project (INtegrated SPECT/MRI for Enhanced Stratification in Radio-chemo Therapy). The project aims to realize two prototypes, the first one dedicated to preclinical imaging on mouse and rat brains (MRI: 7 and 9.4 T, bore diameter: 20 cm), the second one for clinical studies on patients (MRI: 3 T, bore diameter: 59 cm).

II. Proposed Photo-Detection System Design

The photo-detection module proposed for INSERT is designed on the well-established Anger architecture [13], with a continuous CsI:Tl scintillator read by an array of SiPMs, as shown in Fig. 1. The electric signals from SiPMs are conveyed to a multi-channel ASIC and digitized by an external data acquisition system (DAQ). A cooling system is necessary to reduce the dark count rate (DCR) of the SiPMs and to stabilize the multiplication gain. An ASIC board can host a modular number of SiPMs, organized and mounted on custom-designed FR4 boards, called tiles. The desired field of view (FOV) can be achieved by assembling a suitable number of these units. Specifically, the 5 cm × 5 cm FOV in the preclinical system is composed by four tiles, whereas the 10 cm × 5 cm FOV in the clinical is realized with eight tiles. As general strategy, the elements composing the detection module are the same for both SPECT systems, in order to avoid the design of two parallel classes of components. In other words, referring to Fig. 1, for the clinical module the whole detection module is mounted, whilst for the preclinical only half of the camera is equipped.

Preliminary simulations were performed with SCIDRA, an internally developed Monte Carlo code. Details on the program can be found in [14]. Simulation were performed with a 52 mm × 52 mm, 8 mm thick, CsI:Tl scintillator, considering the decay time constants provided for this crystal at room temperature by [15]. Thickness was set to 8 mm as a compromise between spatial resolution and an acceptable absorption efficiency at the energies of interest (140 keV for ^{99m}Tc up to 365 keV for ^{131}I). The crystal was simulated with a white diffusive material on top and lateral sides in order to enhance light collection and as a consequence energy resolution. Interactions at these surfaces were modeled with a Lambert distribution with 95% reflectivity, called diffusive coating in SCIDRA. An optical grease with a refractive index of 1.605 was considered at the interface with photo-detectors.

The scintillator is read by four tiles with an overall number of 36 pixels each one with 8 mm × 8 mm active area. The final number of photoelectrons per each pixel was calculated considering both photo-detection efficiency (PDE) and ballistic deficit (BD). BD is a reduction related to the convolution of the SiPM signal with the electronics impulse response, an RC filter with a time constant of 10 μs. Finally, noise related to dark count rate was added. Centroid algorithms as well as Maximum Likelihood Estimation can be used to evaluate spatial and energy resolution. The pre-clinical photo-detection module should provide at 140 keV (^{99m}Tc) an intrinsic spatial resolution better than 1 mm and an energy resolution between 11% and 15%, depending on the SiPM technology. Excess noise factor was set to 1.3 and dark count rate between 50 ÷ 100 kHz/mm^2.

Although the design has been finalized and all components have been developed, the complete photo-detector module is still under assembly. In particular the data acquisition system is not fully operational yet. In this work we report about the performance of two main elements of the final system: the single SiPM tile and the multi-channel ASIC. These two components were investigated with dedicated and independent setups. For the single tile, which represents only one quarter of the final module, we developed a nine-channels Anger camera with discrete electronics. The tile was coupled to a monolithic CsI:Tl scintillator with the aim to evaluate achievable spatial and energy resolution with a ^{57}Co source. Also the 36-channels ASIC was coupled to the nine pixels tile, so only 9 channels out of 36 were used. Without the DAQ was not possible to read all the channels in parallel, but only one at a time. Hence, we evaluated the spectroscopic capability of the nine channels separately.

III. Materials and Methods

A. Photo-Detector Setup

1) Silicon PhotoMultiplier Tile: The basic photo-detector unit is a 4 mm × 4 mm SiPM, sketched in Fig. 2. The device is realized with FBK's RGB technology with an average DCR of about 800 kHz/mm^2 and a PDE higher than 30% at 550 nm, ideal to read out a CsI:Tl scintillator [16]. PDE is evaluated without crosstalk and afterpulse contributions. The active area of each Avalanche PhotoDiode is 40 μm × 40 μm, as shown in the close-up in Fig. 2, thus with an overall number of 9340 cells per SiPM. The device is electrically isolated with a 40 μm
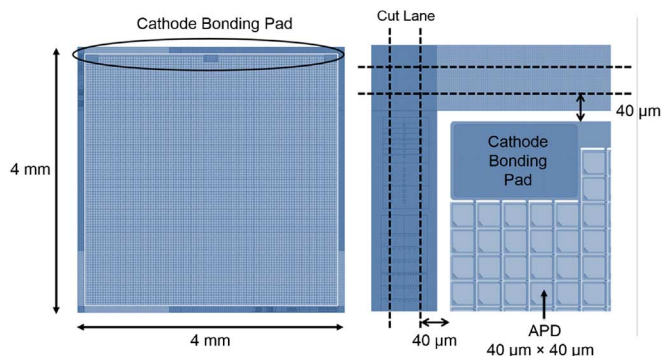
Fig. 2. (Left) Front side of the SiPM device with an area of 4 mm × 4 mm. The cathode pad runs across the entire side of the device to allow bonding wires of adjacent SiPMs. (Right) Close-up of the SiPM showing the single APD cells, the cathode pad and the 40 μm thick frame.

Fig. 4. As shown by the close-up, the mounting is very compact with a distance between the active areas of only 200 μm. The cathodes (front side of the sensor) are connected all together in columns by means of a die-to-die bonding. Then, on the bottom edge of the tile, a wire for each column connects the devices to the board. The columns are shorted together at the board level. The anode of each SiPM (backside of the chip) is independent and routed to a connector placed on the backside of the board.
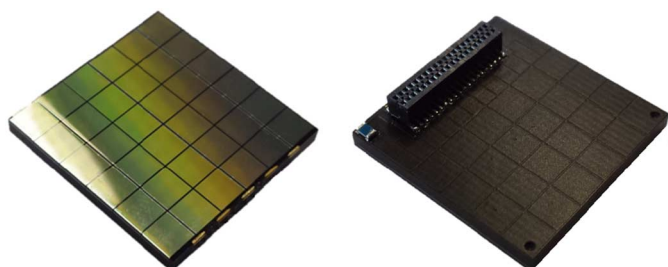

Fig. 3. (Left) Top side of the SiPM module with 36 photo-detectors aligned in a 6 × 6 format. (Right) Bottom side of the module with the socket connector and a PT-100 sensor in one corner to monitor temperature.

Fig. 5. Reverse I-V characteristics of the 36 SiPMs of a tile. The SiPMs show a uniform breakdown voltage, peaked at 29 V.

thick insensitive frame, also used as a safety margin, with a final fill factor equal to 60%.

Each SiPM is characterized by two electrodes: cathode and anode. The cathode provides biasing with typical values between 30-34 V and its pad is realized on the front size of the SiPM. It can be observed in Fig. 2 that this pad extends across the entire side of the SiPM to allow "bridge bonding", as explained in the following. The anode collects the signal for the electronic readout and its pad is realized on the backside of the device, not shown in figure.

As already mentioned, SiPMs are arranged and mounted on highly packed tiles, as shown in Fig. 3. Each tile has 36 SiPMs aligned in a 6 × 6 format and soldered on a 25.30 mm × 25.85 mm, 1.6 mm thick, custom-designed FR4 board. The overall number of pixels of a single tile is reduced from 36 to 9 with a short-circuit of 4 neighbor SiPMs performed on the electronic boards. Thus each tile has nine readout pixels with 8 mm × 8 mm active area as mentioned in the design section. SiPM merging is performed to limit the overall number of electronic channels in the preclinical and clinical systems.

Particular care was taken to minimize insensitive areas between adjacent SiPMs and to provide modularity for larger detection areas. Insensitive area must be carefully avoided, since photon loss can compromise energy resolution. Two main strategies were adopted. i) The biasing for all the detectors is provided through a sequence of bridge bonding wires that connect the cathodes among the top of every SiPM, as shown in Fig. 4. The bonding wires start from five pads positioned on one of the lateral edges of the FR4 board. ii) The precise
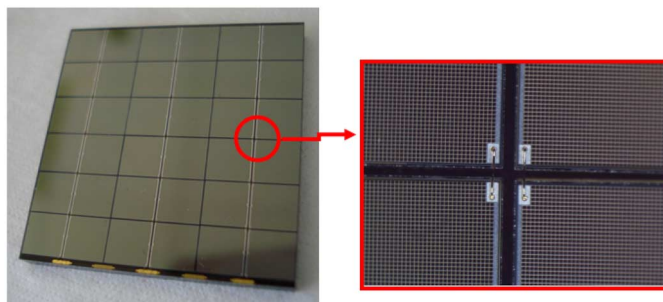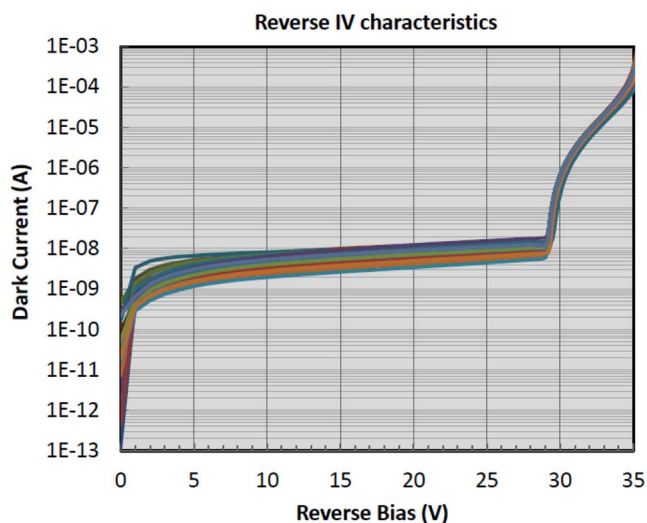
mechanical cut of SiPMs and the alignment on the FR4 board leads to an insensitive thickness, between adjacent SiPMs, of only 200 μm: the already mentioned 40 μm frame and an additional safety margin of 120 μm. Considering also the bonding pads, the gamma-ray detection tile is characterized by only 11.8% of dead area. The tile is covered with an optical resin to maximize light transmission and to protect bonding wires from mechanical damage.

After assembling, the tiles was tested in order to highlight possible failures and malfunctioning and to characterize the tile as well. This functionality testing was mainly performed by means of I-V measurements for each SiPM. Fig. 5 shows the typical reverse Current-Voltage characteristics of the 36 SiPMs. As can be seen from the graph, the breakdown voltage is uniform among the different dies and peaked at 29 V.

2) Scintillator: The tile was coupled to a monolithic CsI:Tl (Scionix, The Netherlands) scintillator by means of a thermoplastic optical media (Meltmount by Cargille) with refractive index of 1.605. The crystal has a 24 mm × 24 mm surface and is 6 mm thick. The top and lateral surfaces were covered with a diffusive material (Telfon). This optical coating solution was
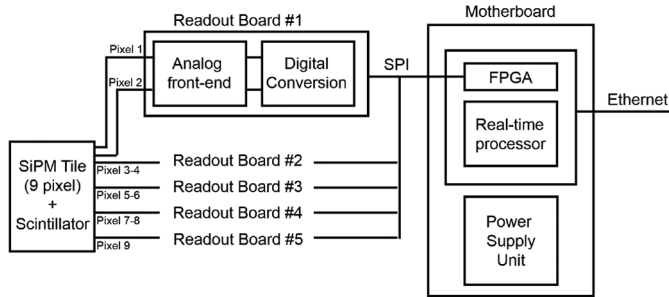
Fig. 6. Scheme of the Anger camera realized with a discrete electronics to evaluate spatial and energy resolution of a single SiPM tile.
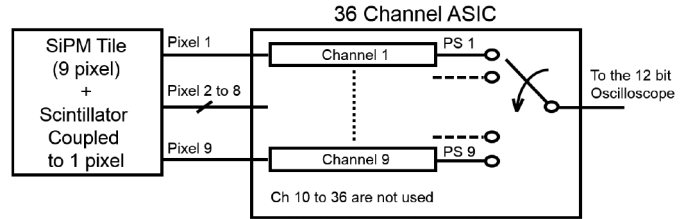

Fig. 7. Scheme of the measurement for the ASIC test. One tile is coupled to nine channels of the ASIC. Only one peak stretcher at a time is available for digitization with a 12 bit oscilloscope.

adopted to achieve the best possible energy resolution at low energies.

3) Cooling: The tile can be cooled by a Peltier element, necessary to reduce the electronic noise added by the SiPMs. The heat generated by the Peltier stage is extracted by a copper block with water circulation. The complete device is enclosed by an aluminum box with humidity controlled to prevent undesired effects. Temperature of the photo-detector was monitored with a Pt-100 sensor mounted on the back of the tile.

4) Readout Electronics: A scheme of the complete system is shown in Fig. 6. Five readout boards, each one with two channels, feature both the analog front-end and the digital section. The current pulses generated by each single channel are integrated by a trans-impedance amplifier with a 10 μs time constant. The integrated signal is held by a peak stretcher stage and finally converted by a 12-bit ADC. The start of conversion of all nine channels is given by a trigger generated by the first channel exceeding a programmable threshold, usually set well above the noise level.

The five readout boards are stacked into a motherboard, which includes both the power supply unit and the data acquisition system. Digitized data are collected by an SPI (Serial Peripheral Interface) bus, routed on the motherboard to an embedded control and acquisition board. This board integrates a real-time processor and a user-reconfigurable FPGA on a single PCB, which is mounted on the motherboard through a high-density connector. Pre-processed data are sent via Ethernet to a PC for elaboration.

5) Data Processing: Per each gamma-ray event nine values Q_i are available. The energy is simply calculated as $E = \sum_{i=1}^{9} Q_i$. If the energy is comprised in a user-defined energy window on the photopeak, the event is accepted, otherwise rejected. The energy window is set $\pm R\%$, where R is the measured energy resolution of the photopeak. If the event is valid, a constant value t is subtracted to all data: $K_i = Q_i - t$. Negative K_i values are set to zero. The number of positive K_i pixels is counted to determine how many pixels, from one to nine, contribute to the reconstruction. If the number of active pixel is below 3, the event is rejected. Finally subtracted values are used for reconstruction with a modified but still simple centroid method:

$$X_C = \frac{\sum_{i=1}^{9} K_i \cdot x_i}{\sum_{i=1}^{9} K_i}, Y_C = \frac{\sum_{i=1}^{9} K_i \cdot y_i}{\sum_{i=1}^{9} K_i} \qquad (1)$$

where (X_C, Y_C) are the coordinates of the gamma event, Q_i is the charge measured by the i-th pixel, (x_i, y_i) the coordinates of i-th pixel center. The value of the baseline t is set to optimize spatial resolution.

B. ASIC Setup

Considering the high number of channels required for the final SPECT system, we designed and developed ANGUS, a 36-channels readout ASIC in standard CMOS 0.35 μm technology (from austriamicrosystem). Particular effort was dedicated to minimize the reciprocal interference between MRI system and electronics. All the communications between ASIC and DAQ exploit balanced signals. Analog outputs from the multiplexer are differential and digital signals are LVDS standard. Since the DAQ was not fully operational for measurements, only one channel at a time was available at the output of the ASIC for conversion. The ASIC was coupled to the tile, so nine pixels for nine readout channels, and for each one a separate spectrum was measured. A scheme of the measurement setup is shown in Fig. 7.

1) Tile and Scintillator: A cylindrical CsI:Tl (Scionix, The Netherlands) scintillator with optical resin (Meltmount) with refractive index of 1.605 was used. The crystal has an 8 mm diameter and is 10 mm thick. The top and lateral surfaces are covered with a diffusive material (Telfon). The scintillator can be coupled to one of the nine available pixels of the tile.

2) ASIC Architecture: The architecture of the single channel is reported in Fig. 8. The current conveyor input stage [17] ensures a high-fidelity scaled reproduction of the current waveform output of the SiPM even in presence of large area detectors, characterized by overall parasitic capacitance with values up to 5 nF in the case of 8 mm × 8 mm pixels. This approach allows to easily adjust the signal amplitude to the dynamic range of the circuit, thus guaranteeing the possibility to exploit very different types of SiPMs. Finally, it gives the possibility to independently tune the input voltage at each channel input, in order to compensate for possible non-uniformity across the detector matrix.

The current conveyor is followed by a programmable RC circuit with the purpose of integrating the input signal and of reducing the impact of the SiPM dark count on the measurement. It can filter the current signal with eight selectable characteristic times ranging from 200 ns to 10 μs, allowing for an effective treatment of signals generated by scintillator crystals with a large range of decay times, though CsI:Tl is our primary choice. The RC filter time constant was set to 10 μs for measurements.
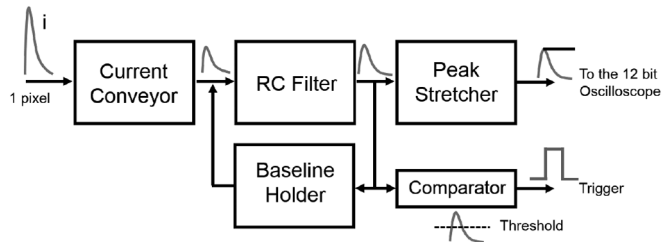
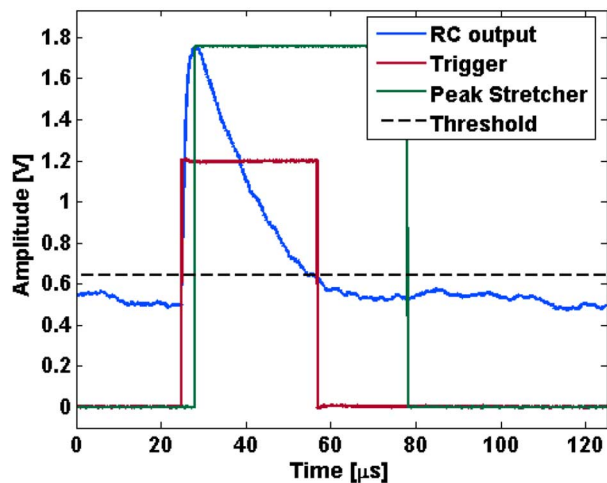Fig. 8. Schematic structure of the single channel of ANGUS.

Fig. 9. Waveform of a single ASIC channel coupled to an 8 mm × 8 mm SiPM pixel. When the output signal of the RC filter overcomes the threshold (dashed), a trigger is provided. The maximum amplitude of the RC filter is held by the peak stretcher for digitization.
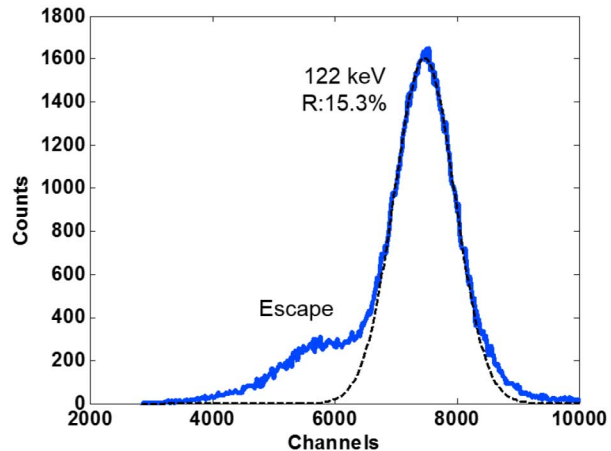

Fig. 10. Typical energy spectrum with a ^{57}Co source with a 15.3% energy resolution at 122 keV peak. This measurement was performed at 0°C to reduce the impact of the dark count rate on energy resolution.

A baseline holder circuit sets the baseline voltage to a defined value, in principle without regard to the input rate of events [18].

The signal is fed at the same time to a comparator and a peak stretcher [19]. The comparator has a programmable threshold set by an internal DAC and provides a trigger when the signal overcomes the threshold as shown in Fig. 9. If a trigger is generated, the peak stretcher circuit stores the maximum amplitude of the signal and feeds it to an analog multiplexer, whose output can be connected to an external ADC on the DAQ board. Since multiplexing is controlled by the DAQ, the parallel acquisition of all the channels was not possible. Only one peak stretcher selectable among all the others by an internal switch was available at the output for digitization. Data conversion was performed by a 12-bit oscilloscope (Waverunner HRO 64zi by Lecroy).

IV. RESULTS

A. Detector Measurements

The system described in Section III(A) was cooled down to 0°C in order to decrease the DCR from $\sim$ 800 kHz/mm^2 at room temperature to approximately $\sim$ 200 kHz/mm^2. Overvoltage was optimized to obtain the best energy resolution and was set to 32 V for all the measurements reported in this section. Energy resolution was evaluated irradiating the camera with an uncollimated ^{57}Co source placed at a distance of 40 cm from

the top of the scintillator. The measured spectrum is reported in Fig. 10, the programmable threshold was set to have at least an energy corresponding to 3000 channels. Energy resolution was calculated by means of a Gaussian fitting (FWHM) on the 122 keV peak with a value of 15.3%.

Spatial resolution was estimated placing a lead grid on the top side of the scintillator. The grid is 4 mm thick, each hole has 1 mm diameter with a pitch from hole to hole of 4 mm. The ^{57}Co source was positioned at 40 cm from the grid to grant a quasi-uniform irradiation through the holes. Fig. 11 Top) shows the events comprised in a $\pm15\%$ energy window on the 122 keV photopeak. The grid pattern is clearly visible and the different holes are distinguishable in the central part of the FOV. At the lateral sides, the image is affected by compression, related to centroid method. Spatial resolution (FWHM) was calculated by means of a Gaussian fitting for both x and y axes and corrected for non-linearity. The average spatial resolution evaluated for the nine central spots in Fig. 11 Top) was evaluated to be approximately 2 mm. The average peak-to-valley ratio for the line profile shown in Fig. 11 Bottom) was 4.6:1.

B. Measurements with a Single ASIC Channel

The performance of the nine channels coupled to the tile was evaluated by moving the cylindrical scintillator to the corresponding 8 mm × 8 mm pixel and by acquiring a ^{57}Co spectrum. Measurements were performed at room temperature since the effect of DCR in this configuration has small impact on the final result. Overvoltage was set to 31.8 V.

Energy resolution was evaluated irradiating the camera with an uncollimated ^{57}Co source placed at a distance of 5 cm from the scintillator. Calibration from channels to keV was performed with a linear interpolation of the 14 keV and 122 keV peaks. Saturation of the SiPM was not taken into account since CsI:Tl is a slow scintillator and the number of available cells is higher than the number of photons for this energy. Energy resolution was calculated for each of the nine channels by means of a Gaussian fitting (FWHM) on the 122 keV peak with values ranging from
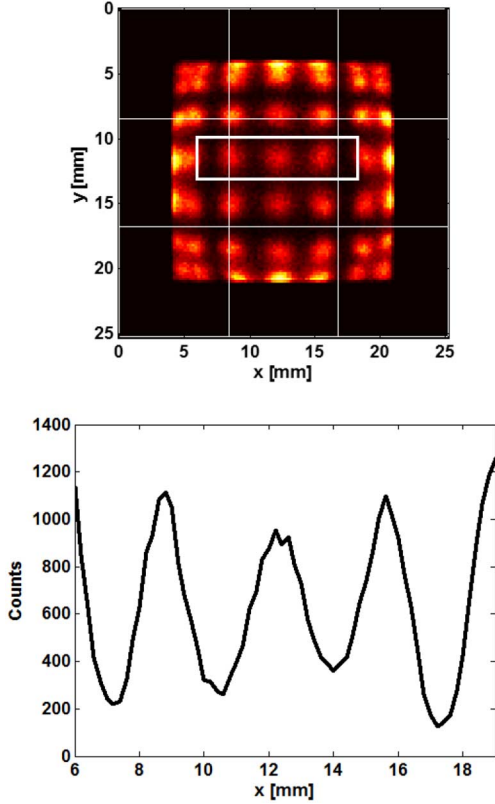
Fig. 11. Top) Imaging reconstruction using modified centroid method with baseline subtraction. The grid is clearly visible and the different spots are distinguishable in the central part of the FOV. At the lateral sides, the image is affected by compression. The measurement was performed at $0°$C. Bottom) Line profile for the row inside the box shown in the reconstruction image.
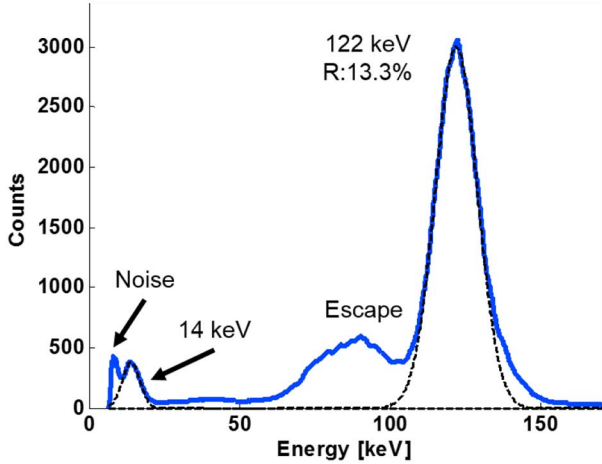

Fig. 12. Spectrum of ^{57}Co measured at the output of peak stretcher. The 14 keV and 122 keV peaks are visible, with a 13.3% resolution at 122 keV. The measurement was performed at room temperature.

13% to 13.5%. Fig. 12 shows for example the spectrum measured with central pixel of the tile, providing a resolution of 13.3% for the 122 keV peak.

V. DISCUSSION

This work investigated preliminary performance of two main components of a proposed photo-detection module for SPECT/MRI applications. The SiPM tile and the readout ASIC were tested separately with different setups. We developed and tested a first prototype of gamma-camera based on a single SiPM tile with nine pixels each with an active area of 8 mm $\times$ 8 mm First gamma-ray imaging results show a 15.3% energy resolution at 122 keV and an average spatial resolution of 2 mm in the central part of the FOV, when the tile is cooled at $0°$C to reduce the impact of DCR. This result is not suitable for small animal imaging, but the measurements are not truly representative of the final performance of the INSERT gamma-ray module for several reasons. Monte Carlo simulations were performed in different conditions, with four tiles and 36 pixels, a slightly higher gamma-ray energy (140 keV) and much lower DCR ($50 \div 100$ kHz/mm^2). Measurements were performed at an equivalent DCR of 200 kHz/mm^2, still high for low-energy imaging. Only nine pixels were used, leading to a poor sampling of the light distribution inside the scintillator. Moreover, this distribution is worsened by reflections on lateral sides due to the limited ratio between lateral side (26 mm) and thickness (6 mm).

Furthermore, we designed a low-noise 36-channels ASIC for SiPM readout. We tested the spectroscopy capability of single readout channels of the ASIC, measuring for example 13.3% resolution at room temperature.

A qualitative explanation of the energy resolution R at a given energy E obtained in the two configurations can be provided by the related formula [20]:

$$R(E) = 2.355 \sqrt{\left(\frac{\Delta E}{E}\right)^2_{int} + \frac{ENF}{N_{pe}} + \left(\frac{ENC}{N_{pe}}\right)^2} \quad (2)$$

here $(\Delta E \backslash E)_{int}$ is the intrinsic resolution of the scintillator, related to non-proportional response of the crystal. The second term is the statistical spread of the number of photo-electrons N_{pe} generated by the SiPMs, possibly worsened by the excess noise factor (ENF) of the multiplication process. The third term is the contribution given by the electronic noise of the detectors and readout chain. The equivalent noise charge ENC, expressed in r.m.s. electrons, is proportional to the square root of the DCR on the overall area. In first approximation, the only contribution that scales with the area from single 8 mm $\times$ 8 mm channel to nine channels is the electronic noise. As DCR halves every $8 \div 10°$C, it is possible to say that the overall DCR of nine channels, cooled down at $0°$C, is equivalent to roughly two channels at room temperature. As a consequence 15.3% resolution of nine channels is comparable with 13.3% of the single channel.

Some technical considerations about INSERT design are discussed in the following. The adoption of Anger architecture for the detection module should grant a reasonable spatial intrinsic resolution in the order of 1 mm, with a simple detector configuration and a limited number of channels with respect to a pixelated approach. This advantage could be relevant in the translation from preclinical to clinical systems in terms of complexity and cost. This architecture was preferred to alternatives like resistive networks to apply statistical methods to retrieve depth of interaction information and to achieve a larger field of view.

We opted to use CsI:Tl primarily due to its higher light yield compared to other scintillators in order to achieve a reasonable energy resolution at low energies. NaI:Tl could be a suitable alternative thanks to its short decay time, but according to our simulations it provides a worse energy resolution due to its lower light yield. Other materials were discarded for both poor intrinsic energy resolution and low light yield or MRI incompatibility, for example LYSO:Ce [21] and GaGG:Ce [22] [23].

The main disadvantage of CsI:Tl is its slow decay time with worse performance at lower temperature [24], [15]. A slow input signal requires few microseconds of integration time to maximize the signal-to-noise ratio, with values ranging from 5 μs to 10 μs depending on several factors, such as shape of the analog filter, dark count rate, temperature of operation and gamma-ray energy. As a direct consequence, count rate capability will be limited to $10 \div 15$ kcps per detection module, according to simulations. Experimental characterization is required for confirmation.

In the proposed monolithic approach, the electronic noise generated by the SiPMs is the most limiting factor for both spatial and energy resolution. An equivalent DCR of $50 \div 100$ kHz/mm^2 is still mandatory to obtain the simulated 1 mm spatial resolution and can be achieved by the combined effect of both a better SiPM technology and of a proper cooling system. The new FBK's RGB-HD (High Density) technology is replacing the current RGB process with higher fill factor and lower DCR. An MRI-compatible cooling system is a challenge in itself, considering that each module must be cooled down to $0 \div 5°$C. Non magnetic material such as conductive plastic or ceramic and non-leaking fluids like compressed air are under test for this purpose.

VI. CONCLUSION

In this work we have investigated the preliminary performance of the SiPM photo-detector unit and of the multi-channel ASIC in the framework of the INSERT project.

REFERENCES

[1] S. R. Cherry, "Multimodality imaging: Beyond PET/CT and SPECT/CT," *Seminars Nucl. Med.*, vol. 39, pp. 348–353, Sep. 2009.

[2] S. R. Meikle, P. Kench, M. Kassiou, and R. Banati, "Small animal SPECT and its place in the matrix of molecular imaging technologies," *Phys. Med. Biol.*, vol. 50, pp. R45–R61, Oct. 2005.

[3] C. Goetz, E. Breton, P. Choquet, V. Israel-Jost, and A. Constantinesco, "SPECT low-field MRI system for small-animal imaging," *J. Nucl. Med.*, vol. 49, pp. 88–93, Jan. 2008.

[4] E. Breton, P. Choquet, C. Goetz, J. Kintz, P. Erbs, R. Rooke, and A. Constantinesco, "Dual SPECT/MR imaging in small animal," *Nucl. Instrum. Methods Phys. Res. A*, vol. 571, pp. 446–448, Feb. 2007.

[5] B. M. W. Tsui, J. W. Hugg, J. Xu, S. Chen, D. Meier, W. Edelstein, A. El-Sharkawy, D. J. Wagenaar, and B. E. Patt, "Design and development of MR-compatible SPECT systems for simultaneous SPECT-MR imaging of small animals," *Proc. SPIE*, vol. 7961, p. 79611Y, Mar. 2011.

[6] D. Meier, D. J. Wagenaar, S. Chen, J. Xu, J. Yu, and B. M. W. Tsui, "A SPECT camera for combined MRI and SPECT for small animals," *Nucl. Instrum. Methods Phys. Res. A*, vol. 652, pp. 731–734, Oct. 2011.

[7] M. J. Hamamura, S. Ha, W. W. Roeck, L. T. Muftuler, D. J. Wagenaar, D. Meier, B. E. Patt, and O. Nalcioglu, "Development of an MR-compatible SPECT system (MRSPECT) for simultaneous data acquisition," *Phys. Med. Biol.*, vol. 55, pp. 1563–1575, Feb. 2010.

[8] L. Cai, X. Lai, Z. Shen, C.-T. Chen, and L.-J. Meng, "MRC-SPECT: A sub-500 μm resolution MR-compatible SPECT system for simultaneous dual-modality study of small animals," *Nucl. Instrum. Methods Phys. Res. A*, vol. 734, pp. 147–151, Jan. 2014.

[9] C. Bouckaert, S. Vandenberghe, and R. V. Holen, "Evaluation of a compact, high-resolution SPECT detector based on digital silicon photomultipliers," *Phys. Med. Biol.*, vol. 59, pp. 7521–7539, Nov. 2014.

[10] M. Georgiou, G. Borghi, S. V. Spirou, G. Loudos, and D. R. Schaart, "First performance tests of a digital photon counter (DPC) array coupled to a CsI(Tl) crystal matrix for potential use in SPECT," *Phys. Med. Biol.*, vol. 59, pp. 2415–2430, Apr. 2014.

[11] S. Yamamoto, J. Y. Yeom, K. Kamada, T. Endo, and C. Levin, "Development of an ultrahigh resolution block detector based on 0.4 mm pixel Ce:GAGG scintillators and a silicon photomultiplier array," *IEEE Trans. Nucl. Sci.*, vol. 60, no. 6, pp. 4582–4587, Dec. 2013.

[12] S. David, M. Georgiou, E. Fysikopoulos, and G. Loudos, "Evaluation of a SiPM array coupled to a $Gd_3Al_2Ga_3O_{12}$:Ce (GAGG:Ce) discrete scintillator," *Phys. Med.*, vol. 15, pp. S1120–1797, Apr. . 2015.

[13] H. O. Anger, "Scintillation camera," *Rev. Sci. Instrum.*, vol. 29, pp. 27–33, Oct. 1958.

[14] L. Boschini and C. Fiorini, "SCIDRA: A monte carlo simulator for the study and optimization of gamma cameras based on a scintillator coupled to a silicon photodetector array," in *Proc. IEEE Nuclear Science Symp. Conf. Rec.*, Oct. 1999, vol. 1, pp. 464–469.

[15] J. D. Valentine, W. W. Moses, S. E. Derenzo, D. K. Wehe, and G. F. Knoll, "Temperature dependence of CsI(Tl) gamma-ray excited scintillation characteristics," *Nucl. Instrum. Methods Phys. Res. A*, vol. 325, pp. 147–157, Feb. 1993.

[16] N. Serra, A. Ferri, A. Gola, T. Pro, A. Tarolli, N. Zorzi, and C. Piemonte, "Characterization of new FBK SiPM technology for visible light detection," *J. Instrum.*, vol. 8, pp. 3–19, Mar. 2013.

[17] F. Corsi *et al.*, "BASIC: An 8-channel front-end ASIC for silicon photomultiplier detectors," in *Proc. IEEE Nuclear Science Symp. Conf. Rec.*, 2009, pp. 1082–1087.

[18] G. D. Geronimo, P. O'Connor, and J. Grosholz, "A CMOS baseline holder (BLH) for readout ASICs," *IEEE Trans. Nucl. Sci.*, vol. 47, no. 3, pp. 818–822, Jun. 2000.

[19] M. W. Kruiskamp and D. M. W. Leenaerts, "A CMOS peak detect sample and hold circuit," *IEEE Trans. Nucl. Sci.*, vol. 41, no. 1, pp. 295–298, Feb. 1994.

[20] M. Moszynski, C. Plettner, A. Nassalski, T. Szczesniak, L. Swiderski, A. Syntfeld-Kazuch, W. Czarnacki, G. Pausch, J. Stein, A. Niculae, and H. Soltau, "A comparative study of silicon drift detectors with photomultipliers, avalanche photodiodes and PIN photodiodes in gamma spectrometry with LaBr$_3$ crystals," *IEEE Trans. Nucl. Sci.*, vol. 56, no. 3, pp. 1006–1011, Jun. 2009.

[21] W. Chewpraditkul, L. Swiderski, M. Moszynski, T. Szczesniak, A. Syntfeld-Kazuch, C. Wanarak, and P. Limsuwan, "Scintillation properties of LuAG:Ce, YAG:Ce and LYSO:Ce crystals for gamma-ray detection," *IEEE Trans. Nucl. Sci.*, vol. 56, no. 6, pp. 3800–3805, Dec. 2009.

[22] J. Iwanowska, L. Swiderski, T. Szczesniak, P. Sibczynski, M. Moszynski, M. Grodzicka, K. Kamada, K. Tsutsumi, Y. Usuki, T. Yanagida, and A. Yoshikawa, "Performance of cerium-doped $Gd_3Al_2Ga_3O_{12}$ (GAGG:Ce) scintillator in gamma-ray spectrometry," *Nucl. Instrum. Methods Phys. Res. A*, vol. 712, pp. 34–40, Jun. 2013.

[23] S. Yamamoto, K. Kuroda, and M. Senda, "Scintillator selection for MR-compatible gamma detectors," *IEEE Trans. Nucl. Sci.*, vol. 50, no. 5, pp. 1683–1685, Oct. 2003.

[24] M. Grodzicka, M. Moszynski, T. Szczesniak, W. Czarnacki, M. Szawowolski, L. Swiderski, L. Kazmierczak, and K. Grodzicki, "Characterization of CsI:Tl at a wide temperature range ($-40°$C to $+22°$C)," *Nucl. Instrum. Methods Phys. Res. A*, vol. 707, pp. 73–79, Apr. 2013.